Journal of Geochemical Exploration 230 (2021) 106859

Contents lists available at ScienceDirect

Journal of Geochemical Exploration

journal homepage: www.elsevier.com/locate/gexplo

Distinguishing IOCG and IOA deposits via random forest algorithm based on magnetite composition

Shuang Hong [a], Renguang Zuo [a,*], Xiaowen Huang [b], Yihui Xiong [a]

[a] State Key Laboratory of Geological Processes and Mineral Resources, China University of Geosciences, Wuhan 430074, China
[b] State Key Laboratory of Ore Deposit Geochemistry, Institute of Geochemistry, Chinese Academy of Sciences, Guiyang 550081, China

ARTICLE INFO

Keywords:
IOCG
IOA
Machine learning
Random forest
Mineral exploration

ABSTRACT

Iron oxide-copper-gold (IOCG) and iron oxide-apatite (IOA) are two significant mineral deposit types with similar tectonic settings and hydrothermal alteration characteristics. There are huge differences in the geological setting, alteration system, and ore-forming fluid composition among IOCG and IOA deposits, leading to controversial genesis. Distinguishing between these two deposit types is significant to reveal the origin of IOCG and IOA systems. In this study, random forest (RF) was employed to classify IOCG and IOA deposits based on the chemical composition of magnetite measured by the electron probe microanalyzer (EPMA) and laser-ablation inductively coupled plasma mass spectrometry (LA-ICP-MS). The obtained results show that (1) a relatively high overall classification accuracy (0.76 for EPMA data and 0.91 for LA-ICP-MS) was obtained via the RF, indicating that the elemental composition of magnetite can effectively distinguish IOCG and IOA deposits; (2) the performance of the RF model based on LA-ICP-MS data is better than that of EMPA data, indicating that the application of more geochemical variables is helpful in distinguishing IOCG and IOA deposits; and (3) the elements V, Mg, and Mn in EPMA data, and Si, Mg, and V in LA-ICP-MS data are identified as the key elements for distinguishing IOCG and IOA deposits.

1. Introduction

Iron oxide-copper-gold (IOCG) deposits are one of the main sources of copper (Cu) and gold (Au) in the world. Since the discovery of giant Olympic Dam deposit in Australia, the IOCG deposit category has attracted considerable attention (Hitzman et al., 1992). The understanding of IOCG deposits has gradually deepened over the past two decades (Williams et al., 2005; Groves et al., 2010). These characteristics mainly involve: (1) Cu-sulfide (with or without Au) hydrothermal mineralization; (2) a large amount of magnetite and hematite; (3) the metallogenic age ranged from the Late Archean to the Mesozoic (Williams et al., 2005); (4) the ore body is controlled by widespread brecciation; and (5) diverse alteration system, tectonic background and ore-forming fluid composition (Hitzman et al., 1992; Hitzman and Porter, 2000; Sillitoe, 2003; Williams et al., 2005; Groves et al., 2010; Barton, 2014). Iron oxide apatite (IOA) deposits are widely developed and are also known as Kiruna-type deposit (Geijer, 1931). Its characteristics mainly include: (1) the apatite-containing iron ore lacks mineralization of polymetallic elements other than Ag, Cu, and rare earth elements (Williams, 2010); (2) Ti-poor magnetite is the main iron ore (Huang et al., 2019); (3) the host rocks are mainly intermediate volcanic rocks; and (4) the genesis of IOA deposits is controversial, including hydrothermal (Hitzman et al., 1992; Rhodes and Oreskes, 1999; Sillitoe and Burrows, 2002) and magmatic (Lundberg and Smellie, 1979; Pollard, 2000; Nyström et al., 2008; Westhues et al., 2016, 2017) models. Nystroem and Henriquez (1994) and Velasco et al. (2016) proposed a magmatic model for the formation of IOA deposits in which magnetite was crystallized from high-temperature, volatile-rich oxide melts. Hitzman et al. (1992) suggested that these two types of mineral deposits were very similar in tectonic settings, mineralization and alteration, igneous host rocks, and regarded IOA deposits as a subclass of IOCG deposits. Knipping et al. (2015a, 2015b) proposed that the IOA deposit was formed by the interaction of igneous rock and magmatic hydrothermal, and the IOA deposit probably represents the deeper origin of the Andean IOCG system based on the combination of field observation, trace element geochemistry, and Fe-O stable isotope composition of magnetite particles (Sillitoe, 2003; Barton, 2014). Huang et al. (2019) also highlighted that these two types of mineral deposits are homologous and probably formed under different temperatures and oxygen fugacity in the same system.

* Corresponding author.
E-mail address: zrguang@cug.edu.cn (R. Zuo).

https://doi.org/10.1016/j.gexplo.2021.106859
Received 19 September 2020; Received in revised form 7 July 2021; Accepted 18 July 2021
Available online 21 July 2021

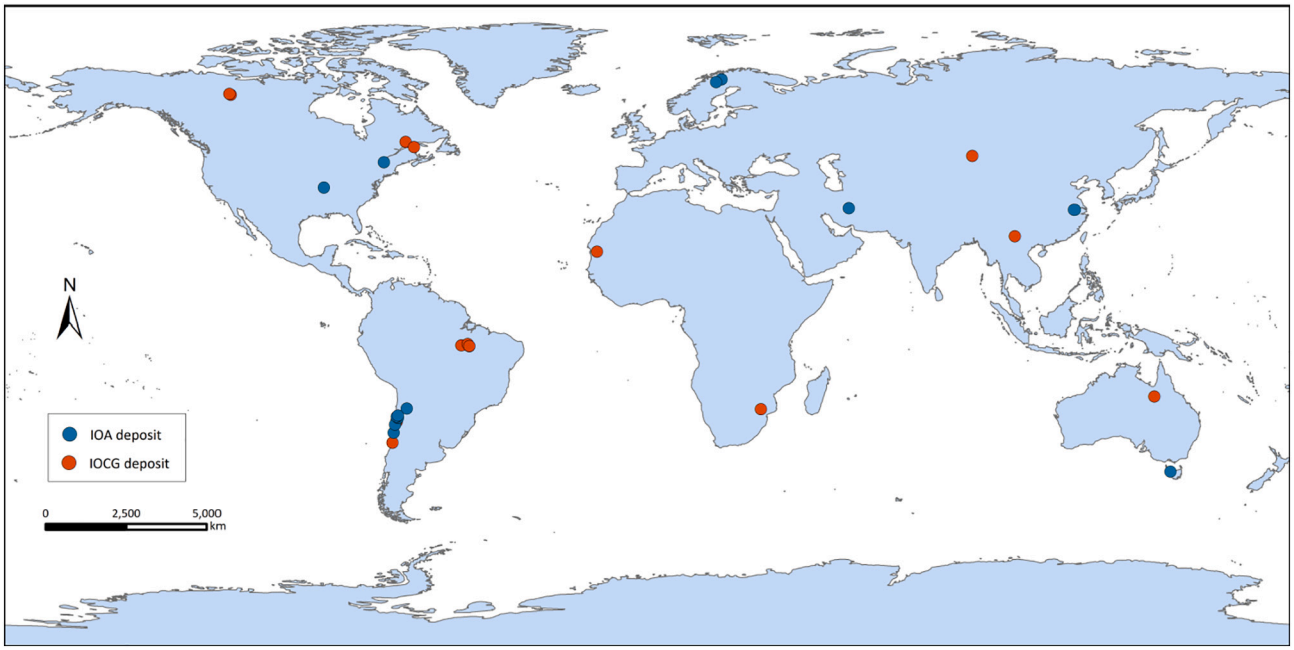

Fig. 1. The spatial distribution of typical IOCG and IOA deposits.
(After Huang et al. (2019))

Magnetite is widely present in magmatic, metamorphic, and sedimentary rocks (Ramdohr, 1980; Scheka et al., 1980), and also in various types of mineral deposits, such as magmatic Fe–Ti–V (P), IOCG, IOA, iron-copper skarn, banded iron formation (BIF), porphyry Cu/Mo/W, and volcanic massive sulfide (VMS) deposits (Leach et al., 2010; Dupuis and Beaudoin, 2011). The factors affecting the composition of magnetite include magma or hydrothermal fluid compositions (Dare et al., 2012; Nadoll et al., 2014; Huang et al., 2016), physical and chemical conditions (e.g., temperature, pressure, cooling rate, and oxygen fugacity, and co-crystallized minerals) (Wechsler et al., 1984; Nadoll et al., 2014; Huang et al., 2019). Magnetite has an inverse spinel structure in which a series of trace elements can replace Fe^{2+} or Fe^{3+} in the magnetite lattice (Buddington and Lindsley, 1964; Nadoll et al., 2014). Owing to its high specific gravity, magnetite cannot be easily transported. The mineral chemistry of magnetite is relatively stable and is not easily affected by low-temperature weathering, thereby preserving its composition (Barnes and Roeder, 2001; Dare et al., 2012, 2014). All these characteristics make magnetite as an important indicator for mineral exploration.

Several diagrams based on the elemental composition of iron oxides have been developed to distinguish IOCG and IOA deposits. For example, Dupuis and Beaudoin (2011) proposed the Ni/(Cr + Mn) vs. Ti + V, and Ca + Al + Mn vs. Ti + V diagrams to distinguish IOCG and IOA deposits from BIF, porphyry, and Fe–Ti–V deposits. Knipping et al. (2015b) applied the V-Cr diagram to identify IOA deposits from IOCG, porphyry, and magmatic Fe-Ti-V deposits. Heidarian et al. (2016) and Broughm et al. (2017) suggested that V vs. Ni, V vs. Ti, V vs. (Ni + Co), and V/Ti vs. Ni/Ti diagrams (Loberg and Horndahl, 1983) are useful for distinguishing IOA deposits from BIF and magmatic Fe-Ti oxide deposits. However, the overlapping limitations are existed in these diagrams (Broughm et al., 2017).

However, these trace element discrimination diagrams are limited in dimension due to the need of visualization (Snow, 2006), or the data used to draw the discriminant diagrams have not been sufficiently encompassed, thus the composition of iron oxides from a single deposit can span multiple areas of the diagrams (Broughm et al., 2017). These result in an unsatisfactory classification performance between IOCG and IOA deposits when the geochemical variables in iron oxides are limited

Table 1
Source and the number of sample of EPMA and LA-ICP-MS.

Deposit name	Number of analyses		Reference
	EPMA	LA-ICP-MS	
IOCG deposits			
IgarapéBahia	27		Huang et al., 2019
Alemao	14	2	Huang et al., 2019
Sossego	56	24	Huang et al., 2019
Alvo 118	13		Huang et al., 2019
Salobo	36	18	Huang et al., 2019
Ernest Henry	37	9	Huang et al., 2019
Candelaria	96	15	Huang et al., 2019; Dupuis and Beaudoin, 2011
Kwyjibo	36	24	Huang et al., 2019
Jatobá	41		Veloso et al., 2020
Mont-de-l'Aigle	14		Dupuis and Beaudoin, 2011
Guelb Moghrein	22		Dupuis and Beaudoin, 2011
Nico	8	26	Dupuis and Beaudoin, 2011; Acosta-Góngora et al., 2014
Punta del Cobre	44		Dupuis and Beaudoin, 2011
Palabora	18		Dupuis and Beaudoin, 2011
Dahongshan		242	Wang et al., 2020
Laoshankou		50	Liang et al., 2020
Sue Dianne		15	Acosta-Góngora et al., 2014
IOA deposits			
Cerro Negro Norte	40	77	Salazar et al., 2020
El Laco	139	16	Dare et al., 2015; Dupuis and Beaudoin, 2011
El Romeral	126	69	Rojas et al., 2018; Huang et al., 2019; Palma et al., 2020
Kiruna	14	4	Huang et al., 2019
Rektorn	13	3	Huang et al., 2019
Savage River	17	3	Huang et al., 2019
Pilot Knob	15		Huang et al., 2019
Lyon Mountain	18		Huang et al., 2019
Gushan		43	Sun et al., 2019
Se–Chahun		5	Bonyadi et al., 2011
Los Colorados		13	Knipping et al., 2015b
Carmen	22	60	Palma et al., 2020
Fresia	16	113	Palma et al., 2020
Mariela	34	85	Palma et al., 2020

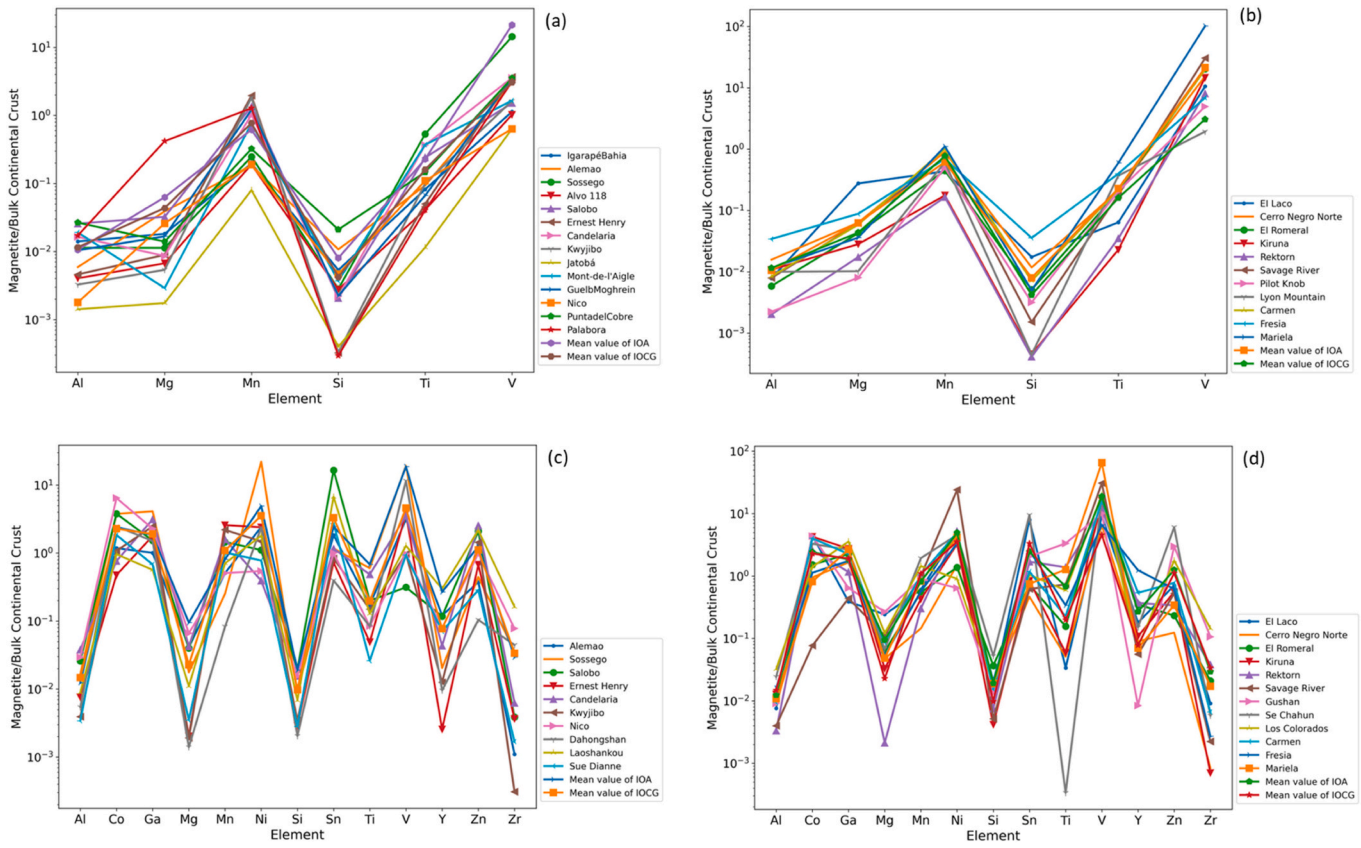

Fig. 2. Multi-element diagrams of average trace element composition of magnetite from individual deposits, normalized to bulk continental crust (Rudnick et al., 2003). The mean value of IOCG/IOA represents the average of all the magnetite elements of the IOCG/IOA deposits collected in this dataset. EPMA data of (a) IOCG and (b) IOA deposits. LA-ICP-MS data of (c) IOCG and (d) IOA deposits.

(Huang et al., 2019). Recent studies suggest that the machine learning methods, such as the partial least squares discriminant analysis (PLS-DA), can help separate IOCG and IOA deposits from VMS, Ni-Cu, porphyry, and VMS-related BIF deposits (Makvandi et al., 2016; Huang et al., 2019).

Random forest (RF), a supervised classifier, is a good choice for classifying a multi-dimensional data source by creating a set of decision trees from a randomly selected subset of the training set. It has been widely used in the field of geosciences (Waske et al., 2009; Gifford and Agah, 2010; Kuhnert et al., 2010; Cracknell and Reading, 2014; Rodriguez-Galiano et al., 2014; Carranza and Laborte, 2015; O'Brien et al., 2015). In the field of geochemistry, Gregory et al. (2019) used LA-ICP-MS pyrite trace element data and RF to distinguish barren sedimentary pyrite and five ore deposit categories: IOCG, orogenic Au, porphyry Cu, sedimentary exhalative (SEDEX), and volcanic-hosted massive sulfide (VHMS) deposits. Therefore, in this study, based on the magnetite geochemistry data, we introduce the RF algorithm for the classification of IOCG and IOA deposits based on the electron probe microanalyzer (EPMA) and the laser-ablation inductively coupled plasma mass spectrometry (LA-ICP-MS) chemical composition.

2. Dataset

The dataset used in this study was compiled from the existing studies (Knipping et al., 2015b; Huang et al., 2019; Palma et al., 2020; Salazar et al., 2020), including 877 magnetite data (462 IOCG and 415 IOA data with 6 geochemical variables) determined by EPMA and 913 magnetite data (425 IOCG and 488 IOA data with 13 geochemical variables) determined by LA-ICP-MS. The samples were collected from 14 IOA deposits and 17 IOCG deposits (Fig. 1). Detailed analytical procedures are available in the references listed in Table 1. Fig. 2 shows the average composition of individual deposits that normalized to bulk continental crust (Rudnick et al., 2003).

The elements of Al, Mg, Mn, Si, Ti, and V in the EPMA dataset and elements of Al, Co, Ga, Mg, Mn, Ni, Si, Sn, Ti, V, Y, Zn, and Zr in the LA-ICP-MS dataset were selected as the preferred input variables. The nearest neighbor function with the Aitchison distance (robcomposition package in *R*) (Hron et al., 2010) was employed to complete the censored values. The centered-log ratio method (Aitchison, 1986) was used to open the closed data.

Fig. 3 shows the notched boxplots of the elemental concentrations of iron oxides in these two datasets. For the EPMA dataset, IOCG deposits have relatively low concentration of Mg, Si, V and similar concentration of Al, Mn, Ti compared with IOA deposits (Fig. 3a). For the LA-ICP-MS dataset, IOCG deposits have relatively lower concentration of Mg, Mn, Si, Sn, Ti, V, Y, and Zn than that of IOA deposits (Fig. 3b).

3. Methods

RF is an ensemble learning-based classification algorithm that is composed of multiple decision trees (Breiman, 2001, Fig. 4). The bootstrap aggregation strategy can overcome the overfitting during the training. *N* samples were randomly selected from the dataset *D* as the training dataset of the decision tree based on bagging method. The decision tree includes the root, branch, and leaf nodes. The nodes of the decision tree were optimally divided. Therefore, the selection of the node splitting mode is significant when constructing a decision tree, as it contributes to the classification of each leaf. The classic classification and decision tree use the Gini coefficient for the determination of the optimal segmentation criteria. The Gini index can be calculated as:

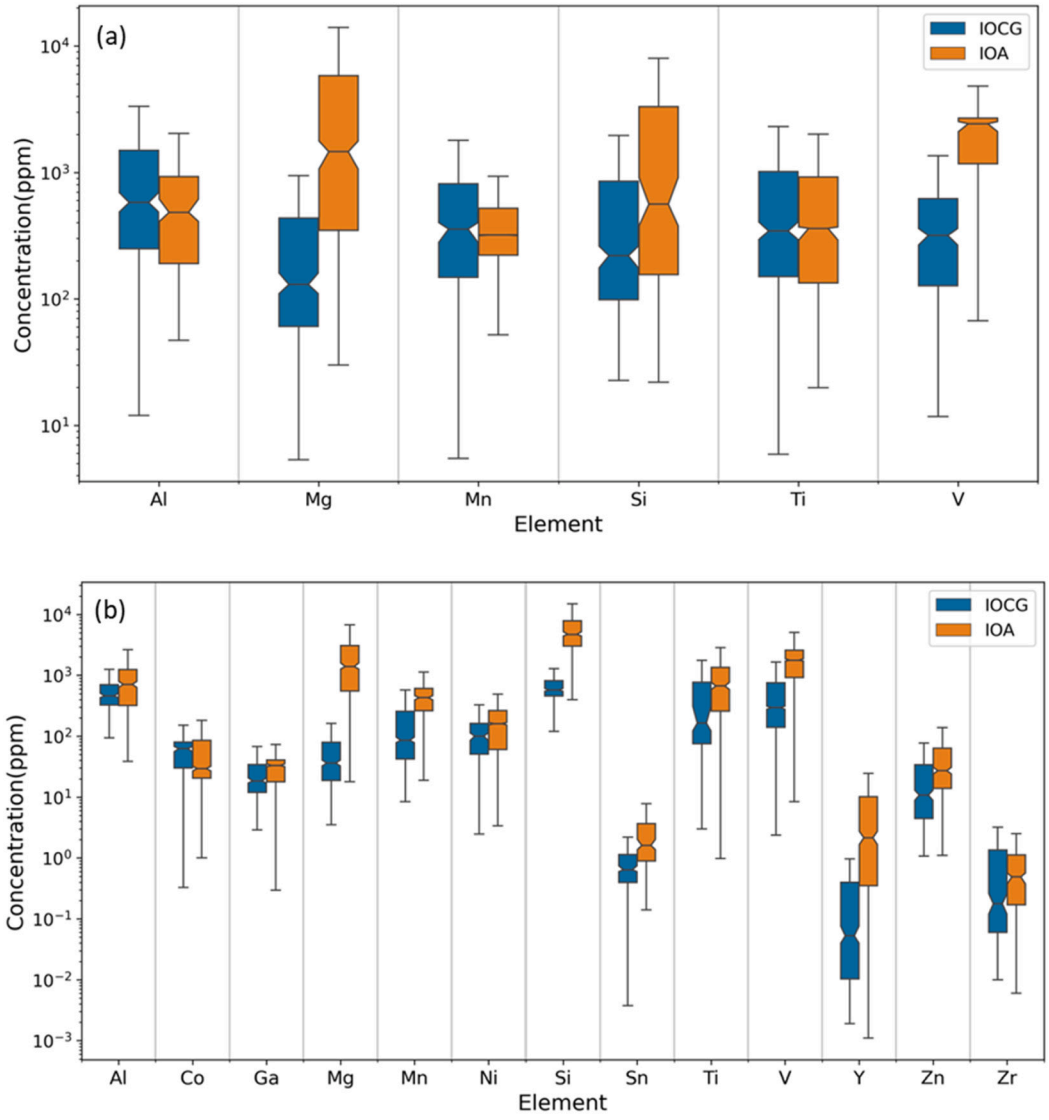

Fig. 3. Notched boxplots of element concentrations of iron oxides measured by (a) EPMA and (b) LA-ICP-MS. The boundaries of the boxes are the 25th to 75th percentiles, he lower whisker is at the lowest datum above Q1 − 1.5 * (Q3 − Q1), and the upper whisker at the highest datum below Q3 + 1.5 * (Q3 − Q1), where Q1 and Q3 are the first and third quartiles. The short lines inside the box represent the median value, and the notches represent the 95% confidence interval of the median.

$$I_G(t) = \sum_{i=1}^{m} f_i(1 - f_i), \tag{1}$$

where m is the class of the dataset and f_i is the probability of class i on the node t.

$$f_i = \frac{g_i}{g}, \tag{2}$$

where g is the total number of samples in node t, and g_i is the number of samples belonging to class C. When all the samples of node t belong to the same class, the Gini index takes the minimum value of 0, and the sample category is purest; when the Gini index takes the maximum value of 1, the sample category in the current node is impure. According to the Gini minimum criterion, each tree splits until all the samples in every subset are correctly classified. The final classification is based on the output of multiple decision trees (Waske et al., 2009; Gregory et al., 2019).

The evaluation of element importance is based on the contribution of each feature to each tree in the RF. The Gini index score of each feature was used as the evaluation index, which represented the change in the Gini index before and after branching. The importance of feature X_j in node t is estimated as:

$$VIM_j(t) = I_G(t) - I_G(s) - I_G(r), \tag{3}$$

$I_G(s)$ and $I_G(r)$ denote the Gini indices of the new nodes s and r after branching, respectively. The node with feature X_j in tree k is the set T, and the importance of X_j in the tree k is

$$VIM_{jk} = \sum_{t \in T} VIM_j(t), \tag{4}$$

When there are N trees

$$VIM_j = \sum_{n=1}^{N} VIM_{jk}, \tag{5}$$

Finally, the importance scores of all the features are normalized to obtain the importance order.

In this study, the RF model was built using Python 3.6.1, and Tensorflow 1.8.0, and scikit-learn library (Pedregosa et al., 2011). The optimal parameters of *n_estimators* (the number of decision trees) and *min_samples_leaf* (the minimum number of samples required at leaf

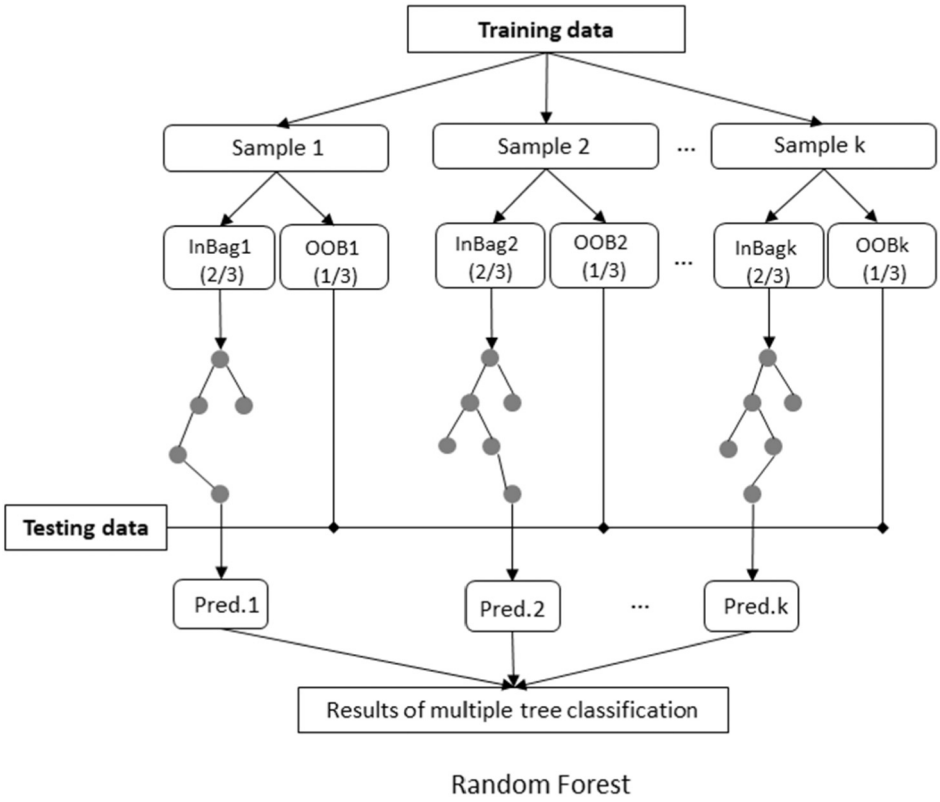

Fig. 4. A workflow of RF. RF builds a number K of decision trees making them grow from different training data subsets, resampling randomly the original data set with replacement. Each decision tree randomly selects 2/3 of the samples from the training set subsets as in bag data for training, and the remaining 1/3 is out of bag data to verify the decision tree. Hence, most data will be used multiple times in different models.

nodes) in a RF model can be obtained through a grid search with cross-validation technique. *Max_features*, is the maximum number of features that can be used by a single decision tree in the RF. *Min_samples_split* is the number of samples required for segmentation.

4. Results and discussion

4.1. Training and testing dataset

In order to train and test the RF model, the magnetite datasets were divided into testing and training datasets. Here, we adopt the leave-one-out method to divide the training and testing datasets. For 25 deposits in the EPMA dataset, one subset was regarded as the testing data, and the other 24 subsets were used as the training dataset. This procedure was then repeated 25 times such that each of the 25 subsets was used exactly once as the testing data. Similarly, one of the 22 deposits in the LA-ICP-MS dataset was used as the testing set, and the remaining 21 deposits were used as the training set. For all the magnetite analysis data in each deposit, the final prediction and classification results of the deposit are determined by getting more votes. For example, if 20 out of the 30 magnetite analyses data of a deposit belong to IOA deposit, the prediction result of the deposit is the IOA deposit. Finally, the classification results for each deposit were obtained to evaluate the classification accuracy of the model.

4.2. Variable importance

For the EPMA magnetite dataset, the importance order of the variables is shown in Fig. 5a. The most important element is V, followed by Mg, Mn, Al, Ti, and Si. V is sensitive to oxygen fugacity. With the increase of oxygen fugacity, its partition coefficient of magnetite decreases (Klemme et al., 2006). The content of V in IOCG was lower than that in IOA, indicating that the sediment of IOCG may be formed at a higher oxygen fugacity than that of IOA. Mg and Mn are suitable for magnetite structures (Dare et al., 2012; Deditius et al., 2018), which may be one of the reasons respond for their high importance. To a certain extent, the geochemistry of magnetite is also affected by host rocks and alteration faces (Huang et al., 2019). Fluid-rock interaction can enrich geochemical elements in hydrothermal fluids, such as magnesium and manganese (Einaudi et al., 1981; Meinert et al., 2005; Huang et al., 2019; Canil and Lacourse, 2020).

The analysis of the importance of geochemistry variables based on LA-ICP-MS data shows that Si, Mg, and V are more important than Ga, Al, Ti, Zn, Co, Zr, and Sn (Fig. 5b). The content of Si is related to the solid solution in the spinel structure, and also exists in the form of small silicate inclusions, which can be easily detected (Ciobanu et al., 2019). Mg and Ti associated with Si may also be derived from the cracking of magmatic silicate and are related to alkaline calcification alteration (Verdugo-Ihl et al., 2020).

4.3. RF classification

For the EPMA dataset, the overall classification accuracy of the 25 deposits was 0.76. Six deposits are misclassified, including two IOCG deposits (Sossego, Palabora) and four IOA deposits (Rektorn, Pilot Knob, Lyon mountain, Fresia) (Table 2). The V content of the Sossego deposit is higher than that of other IOCG deposits, which is closer to the mean value of magnetite collected from IOA deposits. V is an important characteristic of the classifier, which may explain the incorrect classification of IOCG deposits as IOA deposits. Similarly, the Mg content of the Palabora deposit is considerably high, which is close to that of IOA deposit. The elements except V in the Rektorn deposit are lower than other IOA deposits; Mg and Al in the Pilot Knob deposit are lower; V, Mg, and Si in the Lyon mountain deposit are lower; V, Mn, and Mg in the

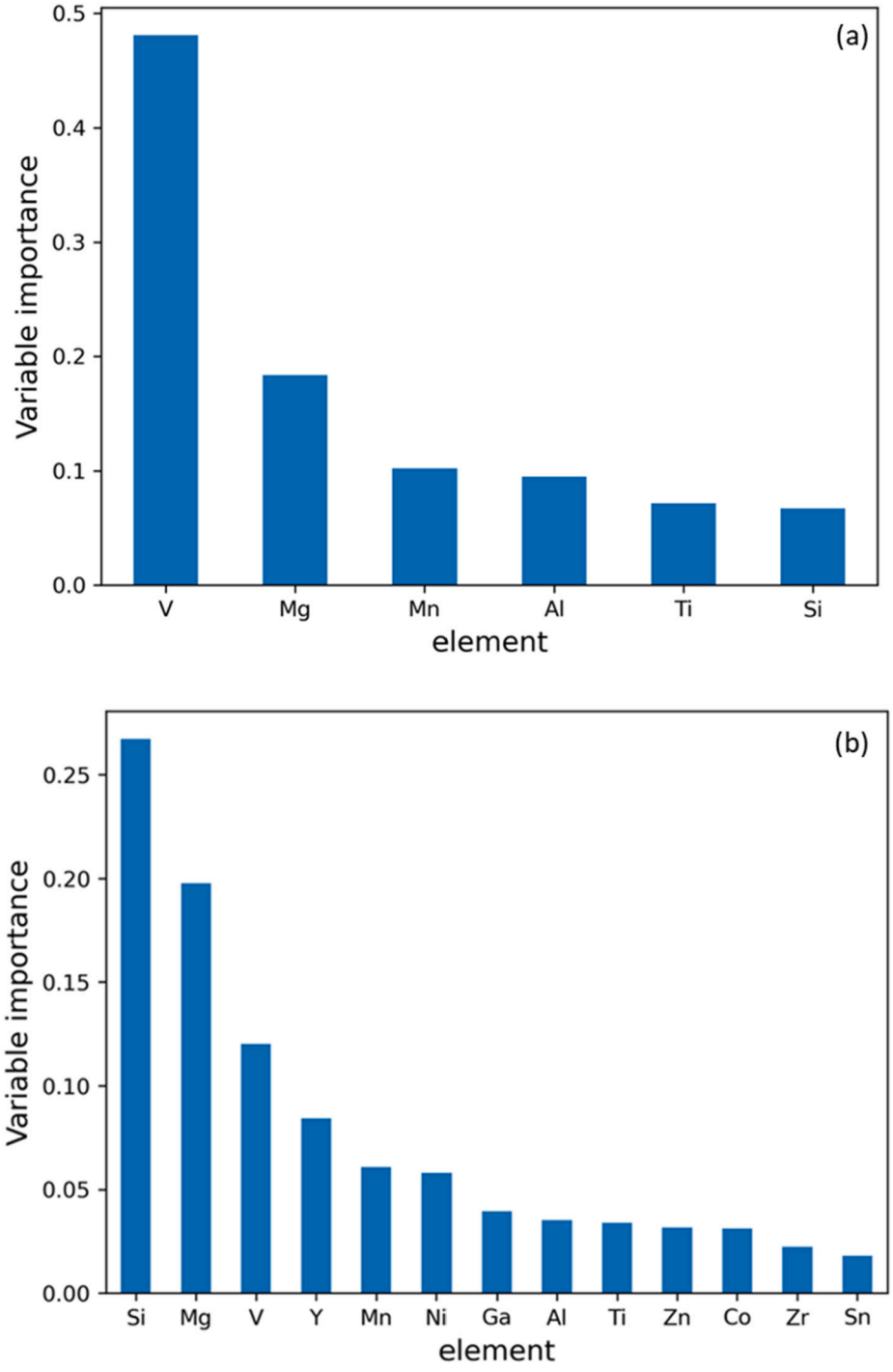

Fig. 5. The importance of variable based on (a) EPMA and (b) LA-ICP-MS dataset.

Table 2
Confusion matrix of random forest classification for all mineral deposit classification results based on EPMA and LA-ICP-MS dataset.

Actual	Predicted	
	IOCG	IOA
EPMA dataset		
IOCG	12	2
IOA	4	7
LA-ICP-MS dataset		
IOCG	8	2
IOA	0	12

Table 3
Confusion matrix of SVM classification for all mineral deposit classification results based on EPMA and LA-ICP-MS dataset.

Actual	Predicted	
	IOCG	IOA
EPMA dataset		
IOCG	11	3
IOA	3	8
LA-ICP-MS dataset		
IOCG	8	2
IOA	1	11

Table 4
Confusion matrix of XGBoost classification for all mineral deposit classification results based on EPMA and LA-ICP-MS dataset.

Actual	Predicted	
	IOCG	IOA
EPMA dataset		
IOCG	12	2
IOA	3	8
LA-ICP-MS dataset		
IOCG	8	2
IOA	2	10

Fresia deposit are similar to other IOA deposits; but Al and Si are high (Fig. 2a, b).

The classification accuracy based on LA-ICP-MS dataset is better than that of EPMA dataset, indicating that more input variables and higher quality data of LA-ICP-MS can play positive role in improving the performance of classification model. The overall classification accuracy of 22 deposits was 0.91, and 2 of 22 deposits misclassify IOCG deposits as IOA deposits (Alemao, Sossego). The Sossego deposit is similar to the EPMA data in that the V element is considerably high, and close to the IOA deposit. The distribution of most elements in Alemao deposit is similar to that of other IOCG deposits, but the Si content is high, which resembles that of the IOA deposit (Fig. 2c, d).

In this study, support vector machine (SVM) (Cortes and Vapnik, 1995) and extreme gradient boosting (XGBoost) (Chen and Guestrin, 2016), which are two popular supervised machine learning algorithms in geosciences (Petrelli and Perugini, 2016; Petrelli et al., 2017; Zhong et al., 2021; Oliveira and Carneiro, 2021), are employed to distinguish IOCG and IOA deposits. The classification accuracy of SVM based on EPMA data is 0.76, and 3 IOCG deposits and 3 IOA deposits are misclassified. The classification accuracy of SVM based on LA-ICP-MS data is 0.86, and 2 IOCG deposits and 1 IOA deposit are misclassified (Table 3). Meanwhile, the classification accuracy of XGBoost based on EPMA data is 0.80, and 2 IOCG deposits and 3 IOA deposits are misclassified. The classification accuracy of XGBoost based on LA-ICP-MS data is 0.82, and 2 IOCG deposits and 2 IOA deposits are misclassified (Table 4).

The experimental results show that although there are complex geochemical patterns of iron oxides in the IOA and IOCG deposits, machine learning can effectively distinguish them. More geochemical data on iron oxide will be collected to build a robust classification model. Furthermore, we will attempt to use machine learning algorithms to distinguish more types of ore deposits according to the elemental concentration of iron oxide. We also aim to use additional machine learning methods to collect more information regarding the formation mechanism of ore deposits, and achieve a deeper understanding of ore deposit formation. The combination of machine learning methods with field work and petrological observation may aid to clearly understand the genesis of the deposit (Petrelli et al., 2017).

5. Conclusions

In this study, the leave-one-out cross validation was used to divide the training and the testing datasets. The RF classifier was employed to classify IOCG and IOA deposits based on the chemical composition of iron oxides measured by the EMPA and LA-ICP-MS. The following conclusions were obtained: (1) although the geochemical composition of iron oxides is complex and uneven, but IOCG and IOA deposits can be distinguished; (2) the training set and testing datasets cannot be divided randomly; they should be divided according to the deposit; (3) the RF model performance based on the LA-ICP-MS dataset is better than the classification model based on EMPA data, indicating that the application of more geochemical variables and higher quality data are useful to distinguish IOA and IOCG deposits; and (4) elements V, Mg, and Mn in the EPMA data, and Si, Mg, V in the LA-ICP-MS data are key to discriminate IOCG from IOA deposits.

CRediT authorship contribution statement

Shuang Hong: Methodology, Formal analysis, Writing - Original draft. **Renguang Zuo:** Conceptualization, Writing - Review & editing, Supervision. **Yihui Xiong:** Writing - Review & editing, Visualization. **Xiaowen Huang:** Data curation.

Declaration of competing interest

The authors have declared that no conflict of interest exists.

Acknowledgements

We thank three reviewers for their comments and suggestions which help us improve this study. This study was supported by the National Natural Science Foundation of China (No. 41772344) and “CAS Hundred Talents Program” project (Y9CJ034000) to XWH.

References

Acosta-Góngora, P., Gleeson, S.A., Samson, I.M., Ootes, L., Corriveau, L., 2014. Trace element geochemistry of magnetite and its relationship to Cu-Bi-Co-Au-Ag-UW mineralization in the Great Bear magmatic zone, NWT, Canada. Econ. Geol. 109, 1901–1928. https://doi.org/10.2113/econgeo.109.7.1901.

Aitchison, J., 1986. In: The Statistical Analysis of Compositional Data. Chapman & Hall, London, pp. 1–416.

Barnes, S.J., Roeder, P.L., 2001. The range of spinel compositions in terrestrial mafic and ultramafic rocks. J. Petrol. 42 (12), 2279–2302. https://doi.org/10.1093/petrology/42.12.2279.

Barton, M.D., 2014. Iron oxide (-Cu-Au-REE-P-Ag-U-Co) systems. In: Treatise on Geochemistry, , Second edition515–541. Elsevier. https://doi.org/10.1016/B978-0-08-095975-7.01123-2.

Bonyadi, Z., Davidson, G.J., Mehrabi, B., Meffre, S., Ghazban, F., 2011. Significance of apatite REE depletion and monazite inclusions in the brecciated Se–Chahun iron oxide–apatite deposit, Bafq district, Iran: insights from paragenesis and geochemistry. Chem. Geol. 281, 253–269. https://doi.org/10.1016/j.chemgeo.2010.12.013.

Breiman, L., 2001. Random forests. Mach. Learn. 45 (1), 5–32. https://doi.org/10.1023/A:1010933404324.

Broughm, S.G., Hanchar, J.M., Tornos, F., Westhues, A., Attersley, S., 2017. Mineral chemistry of magnetite from magnetite-apatite mineralization and their host rocks: examples from Kiruna, Sweden, and El Laco, Chile. Mineral. Deposita 52 (8), 1223–1244. https://doi.org/10.1007/s00126-017-0718-8.

Buddington, A.F., Lindsley, D.H., 1964. Iron-titanium oxide minerals and synthetic equivalents. J. Petrol. 5 (2), 310–357. https://doi.org/10.1093/petrology/5.2.310.

Canil, D., Lacourse, T., 2020. Geothermometry using minor and trace elements in igneous and hydrothermal magnetite. Chem. Geol. 541, 119576 https://doi.org/10.1016/j.chemgeo.2020.119576.

Carranza, E.J.M., Laborte, A.G., 2015. Data-driven predictive mapping of gold prospectivity, Baguio district, Philippines: application of random forests algorithm. Ore Geol. Rev. 71, 777–787. https://doi.org/10.1016/j.oregeorev.2014.08.010.

Chen, T.Q., Guestrin, C., 2016. XGBoost: a scalable tree boosting system. In: The 22nd ACM SIGKDD International Conference on Knowledge Discovery and Data Ming, pp. 785–794. https://doi.org/10.1145/2939672.2939785.

Ciobanu, C.L., Verdugo-Ihl, M.R., Slattery, A., Cook, N.J., Ehrig, K., Courtney-Davies, L., Wade, B.P., 2019. Silician magnetite: Si-Fe-nanoprecipitates and other mineral inclusions in magnetite from the Olympic Dam Deposit, South Australia. Minerals 9 (5), 311. https://doi.org/10.3390/min9050311.

Cortes, C., Vapnik, V., 1995. Support-vector networks. Mach. Learn. 20, 273–297. https://doi.org/10.1007/BF00994018.

Cracknell, M.J., Reading, A.M., 2014. Geological mapping using remote sensing data: a comparison of five machine learning algorithms, their response to variations in the spatial distribution of training data and the use of explicit spatial information. Comput. Geosci. 63, 22–33. https://doi.org/10.1016/j.cageo.2013.10.008.

Dare, S.A., Barnes, S.J., Beaudoin, G., 2012. Variation in trace element content of magnetite crystallized from a fractionating sulfide liquid, Sudbury, Canada: implications for provenance discrimination. Geochim. Cosmochim. Acta 88, 27–50. https://doi.org/10.1016/j.gca.2012.04.032.

Dare, S.A., Barnes, S.J., Beaudoin, G., Méric, J., Boutroy, E., Potvin-Doucet, C., 2014. Trace elements in magnetite as petrogenetic indicators. Mineral. Deposita 49 (7), 785–796. https://doi.org/10.1007/s00126-014-0529-0.

Dare, S.A., Barnes, S.J., Beaudoin, G., 2015. Did the massive magnetite “lava flows” of El Laco (Chile) form by magmatic or hydrothermal processes? New constraints from magnetite composition by LA-ICP-MS. Miner. Deposita 50, 607–617. https://doi.org/10.1007/s00126-014-0560-1.

Deditius, A.P., Reich, M., Simon, A.C., Suvorova, A., Knipping, J., Roberts, M.P., Rubanov, S., Dodd, A., Saunders, M., 2018. Nanogeochemistry of hydrothermal magnetite. Contrib. Mineral. Petrol. 173, 46. https://doi.org/10.1007/s00410-018-1474-1.

Dupuis, C., Beaudoin, G., 2011. Discriminant diagrams for iron oxide trace element fingerprinting of mineral deposit types. Mineral. Deposita 46 (4), 319–335. https://doi.org/10.1007/s00126-011-0334-y.

Einaudi, M.T., Meinert, L.D., Newberry, R.J., 1981. Skarn deposits. In: Economic Geology 75th Anniversary Volume, pp. 317–391.

Geijer, P., 1931. The iron ores of the Kiruna type. Sveriges Geologiska Unders C367, 39.

Gifford, C.M., Agah, A., 2010. Collaborative multi-agent rock facies classification from wireline well log data. Eng. Appl. Artif. Intell. 23, 1158–1172. https://doi.org/10.1016/j.engappai.2010.02.004.

Gregory, D.D., Cracknell, M.J., Large, R.R., McGoldrick, P., Kuhn, S., Maslennikov, V.V., Steadman, J.A., 2019. Distinguishing ore deposit type and barren sedimentary pyrite using laser ablation-inductively coupled plasma-mass spectrometry trace element data and statistical analysis of large dataset s. Econ. Geol. 114 (4), 771–786. https://doi.org/10.5382/econgeo.4654.

Groves, D.I., Bierlein, F.P., Meinert, L.D., Hitzman, M.W., 2010. Iron oxide copper-gold (IOCG) deposits through Earth history: implications for origin, lithospheric setting, and distinction from other epigenetic iron oxide deposits. Econ. Geol. 105 (3), 641–654. https://doi.org/10.2113/gsecongeo.105.3.641.

Heidarian, H., Lentz, D., Alirezaei, S., Peighambari, S., Hall, D., 2016. Using the chemical analysis of magnetite to constrain various stages in the formation and genesis of the Kiruna-type Chadormalu magnetite-apatite deposit, Bafq district, Central Iran. Mineral. Petrol. 110 (6), 927–942. https://doi.org/10.1007/s00710-016-0440-8.

Hitzman, M.W., Oreskes, N., Einaudi, M.T., 1992. Geological characteristics and tectonic setting of proterozoic iron oxide (Cu ± U ± au ± REE) deposits. Precambrian Res. 58 (1–4), 241–287. https://doi.org/10.1016/0301-9268(92)90121-4.

Hitzman, M.W., Porter, T.M., 2000. Iron oxide-Cu-au deposits: what, where, when, and why. In: Hydrothermal Iron Oxide Copper-Gold and Related Deposits: A Global Perspective, 1, pp. 9–25.

Hron, K., Templ, M., Filzmoser, P., 2010. Imputation of missing values for compositional data using classical and robust methods. Comput. Stat. Data Anal. 54 (12), 3095–3107. https://doi.org/10.1016/j.csda.2009.11.023.

Huang, X.W., Gao, J.F., Qi, L., Meng, Y.M., Wang, Y.C., Dai, Z.H., 2016. In-situ LA–ICP–MS trace elements analysis of magnetite: the Fenghuangshan Cu–Fe–Au deposit, Tongling, Eastern China. Ore Geol. Rev. 72, 746–759. https://doi.org/10.1016/j.oregeorev.2015.09.012.

Huang, X.W., Boutroy, É., Makvandi, S., Beaudoin, G., Corriveau, L., De Toni, A.F., 2019. Trace element composition of iron oxides from IOCG and IOA deposits: relationship to hydrothermal alteration and deposit subtypes. Mineral. Deposita 54 (4), 525–552. https://doi.org/10.1007/s00126-018-0825-1.

Klemme, S., Günther, D., Hametner, K., Prowatke, S., Zack, T., 2006. The partitioning of trace elements between ilmenite, ulvospinel, armalcolite and silicate melts with implications for the early differentiation of the moon. Chem. Geol. 234 (3–4), 251–263. https://doi.org/10.1016/j.chemgeo.2006.05.005.

Knipping, J.L., Bilenker, L.D., Simon, A.C., Reich, M., Barra, F., Deditius, A.P., Lundstrom, C., Bindeman, I., Munizaga, R., 2015a. Giant Kiruna-type deposits form by efficient flotation of magmatic magnetite suspensions. Geology 43, 591–594. https://doi.org/10.1130/G36650.1.

Knipping, J.L., Bilenker, L.D., Simon, A.C., Reich, M., Barra, F., Deditius, A.P., Wlle, M., Heinrich, C.A., Holtz, F., Munizaga, R., 2015b. Trace elements in magnetite from massive iron oxide-apatite deposits indicate a combined formation by igneous and magmatic-hydrothermal processes. Geochim. Cosmochim. Acta 171, 15–38. https://doi.org/10.1016/j.gca.2015.08.010.

Kuhnert, P.M., Henderson, A.K., Bartley, R., Herr, A., 2010. Incorporating uncertainty in gully erosion calculations using the Random Forests modeling approach. Environmetrics 21, 493–509. https://doi.org/10.1002/env.999.

Leach, D.L., Bradley, D.C., Huston, D., Pisarevsky, S.A., Taylor, R.D., Gardoll, S.J., 2010. Sediment-hosted lead-zinc deposits in Earth history. Econ. Geol. 105 (3), 593–625. https://doi.org/10.2113/gsecongeo.105.3.593.

Liang, P., Wu, C., Hu, X., Xie, Y., 2020. Textures and geochemistry of magnetite: indications for genesis of the Late Paleozoic Laoshankou Fe-Cu-Au deposit, NW China. Ore Geol. Rev. 124, 103632. https://doi.org/10.1016/j.oregeorev.2020.103632.

Loberg, B.E., Horndahl, A.K., 1983. Ferride geochemistry of Swedish Precambrian iron ores. Mineral. Deposita 18 (3), 487–504. https://doi.org/10.1007/BF00204493.

Lundberg, B., Smellie, J.A.T., 1979. Painirova and Mertainen iron ores: two deposits of the Kiruna iron ore type in northern Sweden. Econ. Geol. 74, 1131–1152. https://doi.org/10.2113/gsecongeo.74.5.1131.

Makvandi, S., Ghasemzadeh-Barvarz, M., Beaudoin, G., Grunsky, E.C., McClenaghan, M. B., Duchesne, C., Boutroy, E., 2016. Partial least squares-discriminant analysis of trace element compositions of magnetite from various VMS deposit subtypes: Application to mineral exploration. Ore Geol. Rev. 78, 388–408. https://doi.org/10.1016/j.oregeorev.2016.04.014.

Meinert, L.D., Dipple, G.M., Nicolescu, S., 2005. World skarn deposits. In: Economic Geology 100th Anniversary Volume, pp. 299–336.

Nadoll, P., Angerer, T., Mauk, J.L., French, D., Walshe, J., 2014. The chemistry of hydrothermal magnetite: a review. Ore Geol. Rev. 61, 1–32. https://doi.org/10.1016/j.oregeorev.2013.12.013.

Nyström, J.O., Billström, K., Henríquez, F., Fallick, A.E., Naslund, H.R., 2008. Oxygen isotope composition of magnetite in iron ores of the Kiruna type in Chile and Sweden. GFF 130 (4), 177–188. https://doi.org/10.1080/11035890809452771.

Nystroem, J.O., Henriquez, F., 1994. Magmatic features of iron ores of the Kiruna type in Chile and Sweden; ore textures and magnetite geochemistry. Econ. Geol. 89 (4), 820–839. https://doi.org/10.2113/gsecongeo.89.4.820.

O'Brien, J.J., Spry, P.G., Nettleton, D., Xu, R., Teale, G.S., 2015. Using Random Forests to distinguish gahnite compositions as an exploration guide to Broken Hill-type Pb–Zn–Ag deposits in the Broken Hill domain, Australia. J. Geochem. Explor. 149, 74–86. https://doi.org/10.1016/j.gexplo.2014.11.010.

Oliveira, L., Carneiro, C., 2021. Synthetic geochemical well logs generation using ensemble machine learning techniques for the Brazilian pre-salt reservoirs. J. Pet. Sci. Eng. 196, 108080 https://doi.org/10.1016/j.petrol.2020.108080.

Palma, G., Barra, F., Reich, M., Simon, A.C., Romero, R., 2020. A review of magnetite geochemistry of Chilean iron oxide-apatite (IOA) deposits and its implications for ore-forming processes. Ore Geol. Rev. 103748 https://doi.org/10.1016/j.oregeorev.2020.103748.

Pedregosa, F., Varoquaux, G., Gramfort, A., Michel, V., Thirion, B., Grisel, O., Blondel, M., Prettenhofer, P., Weiss, R., Dubourg, V., Vanderplas, J., Passos, A., Cournapeau, D., Brucher, M., Perrot, M., Duchesnay, E., 2011. Scikit-learn: machine learning in Python. J. Mach. Learn. Res. 12, 2825–2830. https://www.researchgate.net/publication/305386496.

Petrelli, M., Bizzarri, R., Morgavi, D., Baldanza, A., Perugini, D., 2017. Combining machine learning techniques, microanalyses and large geochemical datasets for tephrochronological studies in complex volcanic areas: new age constraints for the Pleistocene magmatism of Central Italy. Quat. Geochronol. 40, 33–44. https://doi.org/10.1016/j.quageo.2016.12.003.

Petrelli, M., Perugini, D., 2016. Solving petrological problems through machine learning: the study case of tectonic discrimination using geochemical and isotopic data. Contrib. Mineral. Petrol. 171 (10), 1–15. https://doi.org/10.1007/s00410-016-1292-2.

Pollard, P.J., 2000. Evidence of a magmatic fluid and metal source for Fe oxide Cu-au mineralization. In: Hydrothermal Iron Oxide Copper-Gold and Related Deposits: A Global Perspective, 1, pp. 27–41.

Ramdohr, P., 1980. The ore minerals and their intergrowths. Pergamon 1–1207.

Rhodes, A.L., Oreskes, N., 1999. Oxygen isotope composition of magnetite deposits at El Laco, Chile: evidence of formation from isotopically heavy fluids. In: Geology and Ore Deposits of the Central Andes Society of Economic Geologists, 7. Special Publication, pp. 333–351.

Rodriguez-Galiano, V.F., Chica-Olmo, M., Chica-Rivas, M., 2014. Predictive modelling of gold potential with the integration of multisource information based on Random forest: a case study on the Rodalquilar area, Southern Spain. Int. J. Geogr. Inf. Sci. 28 (7), 1336–1354. https://doi.org/10.1080/13658816.2014.885527.

Rojas, P.A., Barra, F., Deditius, A., Reich, M., Simon, A., Roberts, M., Rojo, M., 2018. New contributions to the understanding of Kiruna-type iron oxide-apatite deposits revealed by magnetite ore and gangue mineral geochemistry at the El Romeral deposit, Chile. Ore Geol. Rev. 93, 413–435. https://doi.org/10.1016/j.oregeorev.2018.01.003.

Rudnick, R.L., Gao, S., Holland, H.D., Turekian, K.K., 2003. Composition of the continental crust. Crust 3, 1–64.

Salazar, E., Barra, F., Reich, M., Simon, A., Leisen, M., Palma, G., Romero, R., Rojo, M., 2020. Trace element geochemistry of magnetite from the Cerro Negro Norte iron oxide-apatite deposit, northern Chile. Mineral. Deposita 55 (3), 409–428. https://doi.org/10.1007/s00126-019-00879-3.

Scheka, S.A., Platkov, A.V., Vezhosek, A.A., Levashov, G.B., Oktyabrsky, R.A., 1980. In: The Trace Element Paragenesis of Magnetite. Nauka, Moscow, p. 147.

Sillitoe, R.H., 2003. Iron oxide-copper-gold deposits: an andean view. Mineral. Deposita 38 (7), 787–812. https://doi.org/10.1007/s00126-003-0379-7.

Sillitoe, R.H., Burrows, D.R., 2002. New field evidence bearing on the origin of the El Laco magnetite deposit, northern Chile. Econ. Geol. 97, 1101–1109. https://doi.org/10.2113/gsecongeo.97.5.1101.

Snow, C.A., 2006. A reevaluation of tectonic discrimination diagrams and a new probabilistic approach using large geochemical databases: moving beyond binary and ternary plots. J. Geophys. Res. Solid Earth 111 (B6). https://doi.org/10.1029/2005jb003799.

Sun, W., Yuan, F., Jowitt, S.M., Zhou, T., Liu, G., Li, X., Wang, F., Troll, V.R., 2019. In situ LA–ICP–MS trace element analyses of magnetite: genetic implications for the Zhonggu orefield, Ningwu volcanic basin, Anhui Province, China. Mineralium Deposita 54, 1243–1264. https://doi.org/10.1007/s00126-019-00872-w.

Velasco, F., Tornos, F., Hanchar, J.M., 2016. Immiscible iron-and silica-rich melts and magnetite geochemistry at the El Laco volcano (northern Chile): evidence for a magmatic origin for the magnetite deposits. Ore Geol. Rev. 79, 346–366. https://doi.org/10.1016/j.oregeorev.2016.06.007.

Veloso, A.S.R., Monteiro, L.V.S., Juliani, C., 2020. The link between hydrothermal nickel mineralization and an iron oxide-copper-gold (IOCG) system: constraints based on mineral chemistry in the Jatobá deposit, Carajás Province. Ore Geol. Rev. 121, 103555. https://doi.org/10.1016/j.oregeorev.2020.103555.

Verdugo-Ihl, M.R., Ciobanu, C.L., Cook, N.J., Ehrig, K.J., Courtney-Davies, L., 2020. Defining early stages of IOCG systems: evidence from iron oxides in the outer shell of the Olympic Dam deposit, South Australia. Mineral. Deposita 55, 429–452. https://doi.org/10.1007/s00126-019-00896-2.

Wang, Y.J., Zhu, W.G., Huang, H.Q., Bai, Z.J., Zhong, H., Yao, J.H., Fan, H.P., 2020. Geochemistry of magnetite from the giant Paleoproterozoic Dahongshan Fe-Cu deposit, SW China: constraints on nature of ore-forming fluids and depositional setting. Ore Geol. Rev. 118, 103361. https://doi.org/10.1016/j.oregeorev.2020.103361.

Waske, B., Benediktsson, J.A., Árnason, K., Sveinsson, J.R., 2009. Mapping of hyperspectral AVIRIS data using machine-learning algorithms. Can. J. Remote. Sens. 35, 106–116. https://doi.org/10.5589/m09-018.

Wechsler, B.A., Lindsley, D.H., Prewitt, C.T., 1984. Crystal structure and cation distribution in titanomagnetites (Fe3-xTixO4). Am. Mineral. 69 (7–8), 754–770. https://pubs.geoscienceworld.org/msa/ammin/article/69/7-8/754/104867.

Westhues, A., Hanchar, J.M., Whitehouse, M.J., Martinsson, O., 2016. New constraints on the timing of host-rock emplacement, hydrothermal alteration, and iron oxide-apatite mineralization in the Kiruna District, Norrbotten, Sweden. Econ. Geol. 111, 1595–1618. https://doi.org/10.2113/econgeo.111.7.1595.

Westhues, A., Hanchar, J.M., LeMessurier, M.J., Whitehouse, M.J., 2017. Evidence for hydrothermal alteration and source regions for the Kiruna iron oxide-apatite ore (northern Sweden) from zircon Hf and O isotope. Geology 45, 571–574. https://doi.org/10.1130/G38894.1.

Williams, P.J., Barton, M.D., Johnson, D.A., Fontboté, L., De Haller, A., Mark, G., Oliver, N.H.S., Marschik, R., 2005. Iron oxide copper-gold deposits: geology, space-time distribution, and possible modes of origin. Econ. Geol. 371–405. https://doi.org/10.5382/AV100.13.

Williams, P.J., 2010. Classifying IOCG deposits. In: Corriveau, L., Mumin, H. (Eds.), Exploring for Iron Oxide Copper–Gold Deposits: Canada and Global Analogues, 20. Geological Association of Canada, pp. 13–22. Short Course Notes.

Zhong, R., Deng, Y., Li, W., Danyushevsky, L.V., Cracknell, M.J., Belousov, I., Chen, Y., Li, L., 2021. Revealing the multi-stage ore-forming history of a mineral deposit using pyrite geochemistry and machine learning-based data interpretation. Ore Geol. Rev. 104079 https://doi.org/10.1016/j.oregeorev.2021.104079.